

# Spatio-temporal probabilistic forecast using MMAF-guided learning

Leonardo Bardi, Imma Valentina Curato and Lorenzo Proietti \*

March 17, 2026

## Abstract

We employ stochastic feed-forward neural networks with Gaussian-distributed weights to determine a probabilistic forecast for spatio-temporal raster datasets. The networks are trained using MMAF-guided learning, a generalized Bayesian methodology in which the observed data are preprocessed using an embedding designed to produce a low-dimensional representation that captures their dependence and causal structure. The design of the embedding is theory-guided by the assumption that a spatio-temporal Ornstein-Uhlenbeck process with finite second-order moments generates the observed data. The trained networks, in inference mode, are then used to generate ensemble forecasts by applying different initial conditions at different horizons. Experiments conducted on both synthetic and real data demonstrate that our forecasts remain calibrated across multiple time horizons. Moreover, we show that on such data, simple feed-forward architectures can achieve performance comparable to, and in some cases better than, convolutional or diffusion deep learning architectures used in probabilistic forecasting tasks.

**MSC 2020:** 60E07, 62M20, 60G60, 62C10, 65K10, 68T07.

**Keywords:** spatio-temporal data, feed-forward neural networks, generalized Bayesian posterior, ensemble forecast, calibration.

## 1 Introduction

Raster datasets are (2D) regularly sampled spatio-temporal data that are nowadays generated in environmental monitoring, from satellite observations and socio-economic or demographic studies [24, 30]. Assessing forecast uncertainty for such data is of utmost importance for decision-making. However, this means having access to the so-called (conditional) predictive distribution of the data, which, in the case of a raster dataset, is not explicitly available, given that the data have an unknown spatio-temporal dependence structure and that complex physical dynamics often underlie their generation. Modeling the predictive distribution of the data and having a routine that can sample from it is what we call a *probabilistic forecasting task*. In this paper, we show that *stochastic feed-forward neural networks* can be used for performing such a task.

---

\*TU Chemnitz, Faculty of Mathematics, Reichenhainer Str. 41, 09126 Chemnitz, Germany. E-MAIL:leonardo.bardi@math.tu-chemnitz.de, imma-valentina.curato@math.tu-chemnitz.de, lorenzo.proietti@math.tu-chemnitz.de.

Several state-of-the-art deep learning architectures are in use to determine probabilistic forecasting for spatio-temporal data, such as ConvLSTM [34], ConvGRU [25], DiffSTG [36], and many others, see for a review [6, 23, 37]. Forecasting spatio-temporal datasets, however, entails several limitations when using deep learning architectures, primarily due to the difficulty of fully representing interactions between temporal and spatial dimensions, thereby limiting model performance. For example, accurately capturing spatio-temporal correlation in the data is crucial for enhancing performance in spatio-temporal probabilistic forecasting. On the other hand, focusing solely on this point limits the models’ ability to capture causal relationships in space and time among the random variables that generate the observed dataset. In fact, much of the data we observe consists of records of real physical events occurring at a given location and time. Such events are influenced by neighbouring locations and by past observations, and have an undeniable causal structure that is often not considered by cutting-edge generative algorithms applied to spatio-temporal data. Different approaches are currently being explored in the generative AI community [21]. However, typically, if the model we design can learn causal relationships in the data, it is not well-suited to probabilistic forecasts over multiple time horizons. Moreover, all such networks are computationally very costly. The methodology we present in the paper is designed to overcome these bottlenecks by enabling a careful representation of the spatio-temporal autocorrelation and causal structure in the data. It employs stochastic feed-forward neural networks trained using a novel generalized Bayesian methodology called Mixed Moving Average Field (MMAF, in short) guided learning, introduced in [9].

MMAF-guided learning is a theory-guided methodology, i.e., we assume that a mixed moving average field (MMAF, in short) generates the observed raster dataset. Such a model setup allows modeling the dependence structure of the data without specifying their distribution and incorporates a causal structure represented by a so-called cone-shaped Ambient set [5]. This definition of causality is inspired by the definition of a lightcone in general relativity and, as a causal model, falls within the interpretation given by the potential outcome framework of Rubin [32]. We focus in this work on a specific data generation process called the spatio-temporal Ornstein-Uhlenbeck process (in short, STOU) with finite second moment [28]. This has the effect of focusing on data with exponentially decaying autocorrelation functions along the spatial and temporal dimensions. Other possible model specifications are obviously allowed in MMAF-guided learning, but they are outside the scope of the present paper. We refer the reader to [9, 4] for further details on the possible applications of the methodology to data with a power decaying autocorrelation function (in the case of short and long memory) and to Section 6 for further considerations on non-stationary setups.

The underlying modeling assumption is used to define an embedding of the spatio-temporal index space, which allows us to define features that inherit the field’s dependence structure, expressed using  $\theta$ -lex coefficients, a novel measure of asymptotic dependence introduced in [10], and to provide a causal interpretation. The result of this procedure is obtaining a low-dimensional feature representation of the initial data by using standard statistical techniques, such as the method of moments. The features we create are used to train an ensemble of stochastic feed-forward neural networks (one for each spatial position) with Gaussian-distributed weights. The training is performed using a generalized Bayesian optimization routine [19] based on a PAC Bayesian bound for spatio-temporal  $\theta$ -lex weakly dependent data proven in [9]. The latter bound, unlike the classical ones available in the literature for  $\alpha$ -mixing or  $\theta_{1,\infty}$ -dependent processes, presented in [1] and [2], respectively, can be estimated from observed data.

It is also important to note that using a generalized Bayesian methodology means we do not need to model the likelihood of the data or choose a prior for the feed-forward network parameters in our

framework. Instead, we just need a so-called *reference distribution* that serves as a regularizer in the parameter space [7]. A so-called *generalized posterior distribution* is then directly learned by solving the optimization problem at the base of the training routine. Therefore, our methodology differs from standard Bayesian ones used to analyze spatio-temporal data, as hierarchical Bayes [8, 27], simply because it is not based on the use of the Bayes’ theorem.

The outputs of the trained network at different spatial-time positions determine an *ensemble forecast*. Our ensembles are determined using new input data (not belonging to the training dataset) for each future time horizon we aim to forecast, and given that the data generation is guided by an STOU, they also have a causal interpretation. Our approach to forecasting aligns with what is done, for example, when using weather forecast routines, which, at a specific time interval, use data assimilation of observational data to update the initial conditions of a numerical weather forecast model and produce ensemble forecasts [20, 6]. Such forecasting schemes are suited for data sets that are updated in real time, but whose training phase is very expensive to repeat at each new evaluation time.

We present a complete, feasible workflow for determining ensemble forecasts across multiple time horizons, which also includes validating the *reference distribution* using the continuous ranked probability score (CRPS) of our forecasts [17, 16]. Moreover, we evaluate the calibration of our probabilistic forecast against the predictive distribution of the data by analyzing the empirical quantile ranges and PIT histograms determined from the generated ensemble forecasts. With respect to the generalized Bayesian literature, we use the term calibration in this paper in a different sense than [14, 26]. Here, the authors analyze the calibration of generalized posterior distributions on the parameter space, whereas we analyze whether the outputs of stochastic feed-forward neural networks with parameters sampled from such distributions are calibrated.

We analyze the performance of the generalized Bayesian routine defined in the paper using synthetic and real data sets. The synthetic data sets are generated by a Gaussian and an heavy tail distributed STOU process. The latter has a noise term that is a normal Inverse Gaussian distributed random measure, which we call a Lévy basis. Moreover, we consider the *Outgoing Longwave Radiation Anomalies* (OLR) data set provided by the International Research Institute for Climate and Society. For each considered data set, we compare the probabilistic forecasts obtained with stochastic feed-forward neural networks against the one obtained by using the following state-of-the-art deep learning algorithm: ConvLSTM [34], ConvGRU [25], and DiffSTG [36]. In our empirical study, we observe that our model setup performs better in general than ConvLSTM and ConvGRU, and that the probabilistic forecasts have comparable quality to those produced within a diffusion framework and a lower computational cost in training.

The paper is organized as follows. In Section 2, we describe the modeling assumptions that guide the design of the embedding and the feature extraction routine. In Section 3, we present the optimization problem inspired by a PAC Bayesian bound for  $\theta$ -lex weakly dependent random fields, and the specific design of the training routine for stochastic feed-forward neural networks. We also discuss the inference mode related to the latter and the causal interpretation of the ensemble forecasts. The experimental setup is discussed in Section 4, whereas the performance of MMAF-guided learning applied to our data and the comparisons with state-of-the-art deep learning networks are presented in Section 5. Section 6 concludes.

## 2 Spatio-temporal embedding and features

In this section, we present the theoretical background and the algorithm for defining a spatio-temporal embedding for 2D raster datasets. We indicate random quantities throughout with bold symbols.

### 2.1 Modeling Assumptions

A 2D raster data set is an observed data set  $(\tilde{Z}_t(x))_{(t,x) \in \mathbb{T} \times \mathbb{L}}$  on a regular spatial grid  $\mathbb{L} \subset \mathbb{R}$  across times  $\mathbb{T} = \{t_0 + h_t i : i = 1, \dots, N\}$ , where  $t_0 \in \mathbb{R}$  represents the initial observation time point and  $h_t \in \mathbb{R}$  represents the sample frequency of the data, such that

$$\tilde{Z}_t(x) = \mu_t(x) + Z_t(x) \quad (1)$$

holds, and no measurement errors are present in the observations. Here,  $\mu_t(x)$  is a deterministic function, and  $Z_t(x)$  are considered realizations from a zero mean stationary spatio-temporal Ornstein-Uhlenbeck process, STOU in short, defined as

$$Z_t(x) := \int_{A_t(x)} \exp(-A(t-s)) \Lambda(ds, d\xi), \quad (t, x) \in \mathbb{R} \times \mathbb{R} \quad (2)$$

where  $A > 0$  is called *mean reverting parameter*, and  $A_t(x)$  is defined as

$$A_t(x) := \{(s, \xi) \in \mathbb{R} \times \mathbb{R} : s \leq t \text{ and } \|x - \xi\| \leq c|t - s|\}. \quad (3)$$

$\Lambda$  is a (homogeneous) Lévy basis, i.e. an independently scattered random measure on  $\mathbb{R} \times \mathbb{R}$ . Loosely speaking, the measure associates a random number with any bounded subset  $B$  belonging to the Borel sets  $\mathcal{B}(\mathbb{R} \times \mathbb{R})$ . Whenever two subsets are disjoint, the associated measures are independent, and the measure of a disjoint union of sets almost certainly equals the sum of the measures of the individual sets. We refer to [33] for a more formal definition.

The set  $A_t(x)$  models the causal structure of the random field in space-time. It is formally called an *ambit set*, see [5], and satisfies the following properties.

**Definition 2.1.** *A family of ambit sets  $(A_t(x))_{(t,x) \in \mathbb{R} \times \mathbb{R}}$  is a collection of subsets  $\mathbb{R} \times \mathbb{R}$  which satisfies the following properties:*

1. *translation invariance, i.e.  $A_t(x) = A_0(0) + (t, x)$  for all  $(t, x) \in \mathbb{R} \times \mathbb{R}$ ;*
2.  *$A_s(x) \subset A_t(x)$  for all  $s < t$  and for all  $x \in \mathbb{R}$ ;*
3. *non-anticipative, i.e.  $A_t(x) \cap (t, +\infty) \times \mathbb{R} = \emptyset$*

To explain why a cone-shaped ambit set as defined in (3) introduces a causal structure in space-time, we borrow the interpretation given to a *lightcone* in special relativity. In fact, as a lightcone describes the possible paths that the light can make in space-time, leading to a space-time point and the ones that lie in its future, we use their geometry (in the Euclidean space  $\mathbb{R} \times \mathbb{R}$ ) to identify the space-time points having a causal relationship in the past and the future. The set  $A_t(x)$  corresponds to what we call a *past cone of influence*, whereas the set

$$A_t(x)^+ = \{(s, \xi) \in \mathbb{R} \times \mathbb{R} : s > t \text{ and } \|x - \xi\| \leq c|t - s|\}, \quad (4)$$

is the *future cone of influence* related to the spatial-time point  $(t, x) \in \mathbb{R} \times \mathbb{R}$ . By using an STOU process as the underlying model, we implicitly assume that the following sets

$$l(t, x) = \{\mathbf{Z}_s(\xi) : (s, \xi) \in A_t(x) \setminus (t, x)\} \text{ and } l^+(t, x) = \{\mathbf{Z}_s(\xi) : (s, \xi) \in A_t(x)^+\} \quad (5)$$

are respectively describing the values of the field that have a direct influence on the determination of  $\mathbf{Z}_t(x)$  and the future field values influenced by  $\mathbf{Z}_t(x)$ . We can then infer the causal relationship between space-time points described above by estimating the constant  $c$  from the observed raster data, which we call *the speed of information propagation* in the physical system under analysis. The concept of causality used in the paper can be inscribed in the potential outcome framework described by Rubin in [32].

The STOU is a stationary and Markovian random field. Moreover, an STOU exhibits exponentially decaying temporal autocorrelation (just like the temporal Ornstein-Uhlenbeck process) and has a spatial autocorrelation structure determined by the shape of the ambit set. In addition, this class of fields admits non-separable autocovariances, which are desirable in practice [28]. The STOU is a member of a broader class of random fields called *mixed moving average fields*, MMAF in short, see [9]. All MMAFs are stationary and  $\theta$ -lex-weakly dependent random fields. This means that independently on their distribution we can assess the asymptotic dependence structure of such fields.

**Definition 2.2.** *Let  $\mathbf{Z}$  be an  $\mathbb{R}$ -valued random field. Then,  $\mathbf{Z}$  is called  $\theta$ -lex-weakly dependent if*

$$\theta_{lex}(r) = \sup_{u, v \in \mathbb{N}} \theta_{u, v}(r) \xrightarrow{r \rightarrow \infty} 0$$

where

$$\theta_{u, v}(r) = \sup \left\{ \frac{|Cov(F(\mathbf{Z}_\Gamma), G(\mathbf{Z}_{\Gamma'}))|}{\|F\|_\infty v Lip(G)}, F \in \mathcal{G}_u^*, G \in \mathcal{G}_v, \Gamma, \Gamma', |\Gamma| = u, |\Gamma'| = v \right\}$$

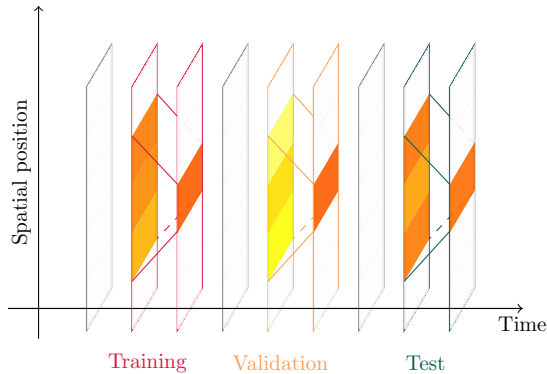
where  $\mathcal{G}_u^*$  represents the set of the bounded functions on  $\mathbb{R}^u$ ,  $\mathcal{G}_v$  the set of bounded and Lipschitz functions on  $\mathbb{R}^v$ ,  $\Gamma, \Gamma' \subset \mathbb{R} \times \mathbb{R}$  space-time points in lexicographic order such that  $dist(\Gamma, \Gamma') = r$ , and where we call the related marginals of the field  $\mathbf{Z}_\Gamma$  and  $\mathbf{Z}_{\Gamma'}$ . We indicate with the sequence  $(\theta_{lex}(r))_{r \in \mathbb{R}^+}$  the  $\theta$ -lex coefficients.

For discrete samples of MMAF, it can be proven that  $\theta$ -lex weak dependence is a more general notion of dependence than  $\alpha$  and  $\phi$ -mixing for spatio-temporal random fields, see Section 2.3 in [10]. Moreover, knowing that the field  $\mathbf{Z}_t(x)$  is  $\theta$ -lex weakly dependent it can be readily proven that the sample  $(\mathbf{Z}_t(x))_{(t, x) \in \mathbb{T} \times \mathbb{L}}$ , generating the observed (zero mean) raster data set, has the same dependence structure.

Hence, by choosing an STOU as the underlying model, we impose that the data respect a given causal structure modeled by the cone-shaped ambit sets and have a dependence structure described by the notion of  $\theta$ -lex weakly dependence. Moreover, we assume throughout that  $\mathbb{E}[|\mathbf{Z}_t(x)|^2] < \infty$ .

We refer to Appendix A for a brief review of the estimation methodology based on the method of moments necessary to estimate the parameter  $A$ ,  $c$ , and the decay rate of the  $\theta$ -lex coefficients of the field. These estimates aim to infer the causal structure and the dependence structure of the observed raster dataset. This estimation step is performed *offline* before training.

Figure 1: Feature extraction with parameters  $c = 1$ ,  $p = 1$ , and  $a = 3$ .



## 2.2 Features Extraction Routine

We design spatio-temporal features as input–output pairs, which are then partitioned into training, validation, and test sets from the 2D observed raster dataset using an embedding of the index set  $\mathbb{T} \times \mathbb{L}$ . W.l.o.g., we will assume that  $h_t = 1$  throughout.

For a given spatio-temporal position  $(t, x^*)$ , we define related features by means of the index set

$$I(t, x^*) = \{(i_s, x_s) \in \mathbb{T} \times \mathbb{L} : |x^* - x_s| \leq c(t - i_s), 0 < t - i_s \leq p\} \quad (6)$$

having cardinality  $D := |I(t, x^*)|$ . Such a set corresponds to a discretization in space and time of the set  $A_t(x)$  defined in (3). The entire number of examples employed in training, validation, and test set represents the *features* we can automatically learn once an embedding is defined. In general, the parameter  $c$  in the definition of the embedding is estimated from the data, see Appendix A,  $p$  is a hyperparameter, and  $a$  is chosen following the rule (11) which is discussed in Section 3.1. We then define the input-output pair  $(X_i, Y_i)$  defined through the index sets  $I(t_0 + ia, x^*)$  for  $i = 1, \dots, \lfloor \frac{N}{a} \rfloor$ , as

$$X_i = (Z_{i_1}(x_1), \dots, Z_{i_D}(x_D))^T \quad Y_i = Z_{t_0+ia}(x^*), \quad (7)$$

where  $(i_s, x_s) \in I(t_0 + ia, x^*)$  and  $(i_s, x_s) <_{lex} (i_{s+1}, x_{s+1})$  for all  $s = 1, \dots, D - 1$ . The symbol  $<_{lex}$  indicates that the point  $(i_s, x_s)$  is in lexicographic order less than  $(i_{s+1}, x_{s+1})$  in  $\mathbb{R} \times \mathbb{R}$ , and the parameters  $a > 0$  and  $p > 0$  are chosen such that  $a \geq p + 1$ . Note that each input vector  $X_i$  corresponds to a sample from  $l(t_0 + ia, x^*)$  defined in (5). Figure 1 represents an example in which the input-output pairs are represented: in this instance, the input vector corresponds to 3 spatial locations.

We call  $S_m = \{(X_i, Y_i)\}_{i=1}^m$  the training data set for a given spatial position  $x^*$  defined through the set  $I(t_0 + ia, x^*)$  for  $i = 1, \dots, m$ . Similarly, the validation set is composed of the input-output pair  $(X_{m+1}, Y_{m+1})$ , which is defined using the embedding  $I(t_0 + (m + 1)a, x^*)$ , and the test set is composed by the input-output pairs  $(X_i, Y_i)$  which is obtain from the sets  $I(t_0 + ia, x^*)$ , for  $i = m + 2, \dots, \lfloor \frac{N}{a} \rfloor$ .

We provide in Algorithm 1 a detailed description of the feature extraction routine. Note that Algorithm 1 varies if we choose a different data generation process or if the dimension of the spatial dimension increases. In [4], for example, a feature extraction routine for 3D raster data sets under the assumption that the data are generated by a *mixed spatio-temporal Ornstein Uhlenbeck process*, defined in [29], can be found.

We call  $\mathbf{S} = (\mathbf{X}_i, \mathbf{Y}_i)_{i \in \mathbb{Z}}$  the stochastic process generating the data described above.  $\mathbf{S}$  is defined on the canonical probability space  $(\Omega, \mathcal{F}, \mathbb{P})$  and it is stationary because of the property of the data generating process (2) where  $(\mathbf{X}_i, \mathbf{Y}_i)$  have values in  $\mathbb{R}^D \times \mathbb{R}$  and are identically distributed.  $\mathbf{S}$  inherits the dependence structure of the field  $\mathbf{Z}$  as proven in Appendix B. Moreover, the geometry of the ambit set enables us to provide a causal interpretation of the forecasts generated using such features in a given spatial position  $x^*$  as discussed in Section 3.2.

---

**Algorithm 1** Feature extraction routine for a spatio-temporal position  $(t, x^*)$ .

---

**Input:**  $(Z_t(x))_{(t,x) \in \mathbb{T} \times \mathbb{L}}$  Raster data consisting of realizations from a (zero mean) STOU process  
 $p$  Hyperparameter (its default value is equal to 1)

1. Estimate the parameters  $A, c, \lambda$  using equations (17) and (18).
2. Select  $a$  as the smallest integer satisfying (11)
3. Define the index sets  $I(t_0 + ia, x^*)$ ,  $i = 1, \dots, \lfloor \frac{N}{a} \rfloor$  following Definition 6.
4. Extract features from  $l(t_0 + ia, x^*)$  having indices in  $I(t_0 + ia, x^*)$ .

**Output:**  $(X_i, Y_i)$  such that

$$X_i = (Z_{i_1}(x_1), \dots, Z_{i_D}(x_D))^{\top} \quad Y_i = Z_{t_0+ia}(x^*),$$

with  $i = 1, \dots, \lfloor \frac{N}{a} \rfloor$ .

---

### 3 MMAF-guided learning for stochastic feed-forward neural networks

In this section, we describe a novel routine for training and inference of stochastic feed-forward neural networks. We call this procedure MMAF-guided learning. We assume throughout that a 2D raster data set is generated by the STOU process (2).

#### 3.1 Optimization and Training

We work with the following class of stochastic feed-forward neural networks. Let 0 and  $\ell + 1$  be the indexes denoting the input and output layers,  $l$  the total number of hidden layers (indexed from 1 to  $\ell$ ),  $D$  the dimension of the input space, and

$$n_0 = D, n_1, \dots, n_\ell, n_{\ell+1} = 1$$

the widths of each layer in the network. We then define for an input  $X_i \in \mathbb{R}^D$

$$h_\theta(X_i) = W^{(\ell+1)} \sigma^{(\ell)}(W^{(\ell)}(\sigma^{(\ell-1)}(W^{(\ell-1)} \dots \sigma^{(1)}(W^{(1)} X_i + b^{(1)}) + b^{(2)} \dots) + b^{(\ell-1)}) + b^{(\ell)}), \quad (8)$$

where the functions  $\sigma^{(1)}, \dots, \sigma^{(\ell)}$  are ReLU activation functions and

$$\theta := (W^{(1)}, \dots, W^{(\ell)}, W^{(\ell+1)}, b^{(1)}, \dots, b^{(\ell)})$$

corresponds to all the weights and bias parameters of the network. We assume in general that  $\theta \in \mathbb{R}^d$ . The class of stochastic feed-forward neural network we work with is then defined as  $\mathcal{H} := \{h_\theta(\cdot) : \theta \sim \mathcal{N}(\mu, \text{diag}(\kappa))\}$ , for  $\mu \in \mathbb{R}^d$  and  $\kappa \in \mathbb{R}_+^d$ .

Let  $S_m := (X_i, Y_i)_{i=1}^m$  be the training data set defined in Section 2.2,  $\epsilon > 0$  be a hyperparameter called the *accuracy level*, we define the truncated absolute loss  $L^\epsilon : \mathbb{R} \times \mathbb{R} \rightarrow [0, +\infty]$ , as  $L^\epsilon(x, y) := |x - y| \wedge \epsilon$ . For a given realization of the parameter  $\theta$ , we define the *population risk*  $R(h_\theta) := \mathbb{E}[L^\epsilon(h_\theta(\mathbf{X}), \mathbf{Y})]$  and the *empirical risk*  $r(h_\theta) := \frac{1}{m} \sum_{i=1}^m L^\epsilon(h_\theta(X_i), Y_i)$  for each  $m \geq 1$ .

We select now a *reference distribution*  $\pi$  on the space  $(\mathbb{R}^d, \mathcal{B}(\mathbb{R}^d))$ , where  $\mathcal{B}(\mathbb{R}^d)$  indicates the Borel  $\sigma$ -algebra on  $\mathbb{R}^d$ . The reference distribution provides a structure on the parameter space  $\mathbb{R}^d$ , which we interpret as our belief that certain parameters are more likely than others to yield better performance. We then learn a distribution over the parameter space *using the observed training data* by solving an optimization problem. We call such distribution a *generalized posterior distribution*  $\rho$  on  $(\mathbb{R}^d, \mathcal{B}(\mathbb{R}^d))$ , and this optimization-centric way of selecting  $\rho$  a *generalized Bayesian algorithm* [19]. Let us first give a more careful definition of the former.

**Definition 3.1.** Let  $\mathcal{G}_m := \sigma(\mathbf{S}_m)$ , where  $\mathbf{S}_m$  is a random vector generating the training data  $S_m$ . We define a *generalized posterior distribution*  $\rho$  as the regular conditional probability distribution of the random variable  $\hat{\mathbf{h}}$  defined on  $(\Omega, \mathcal{F}, \mathbb{P})$  with values in  $(\mathbb{R}^d, \mathcal{B}(\mathbb{R}^d))$  given  $\mathcal{G}_m$ , i.e. for all  $\omega \in \Omega$  and  $E \in \mathcal{B}(\mathbb{R}^d)$

$$\rho(E, \omega) := \mathbb{P}(\hat{\mathbf{h}} \in E | \mathcal{G}_m)(\omega),$$

where

- for any  $E \in \mathcal{B}(\mathbb{R}^d)$ , the function  $\omega \rightarrow \rho(E, \omega)$  is  $\mathcal{G}_m$ -measurable and a variant of the conditional probability  $\mathbb{P}(\hat{\mathbf{h}} \in E | \mathcal{G}_m)$ , i.e.,

$$\rho(E, \cdot) = \mathbb{P}(\hat{\mathbf{h}} \in E | \mathcal{G}_m)(\cdot) \text{ a.s.}$$

- for any  $\omega \in \Omega$ ,  $\rho(\cdot, \omega)$  is a probability measure on  $(\mathbb{R}^d, \mathcal{B}(\mathbb{R}^d))$ .

Second, the optimization problem is defined using the following theoretical result. In [9], a so-called PAC Bayesian bound is proven, which is a bound on the *expected generalization gap* between the *average population and average empirical risk* defined for  $\omega \in \Omega$  as

$$\rho[R(h_\theta)](\omega) - \rho[r(h_\theta)](\omega) := \int_{\mathbb{R}^d} R(h_\theta) \rho(d\theta, \omega) - \int_{\mathbb{R}^d} r(h_\theta) \rho(d\theta, \omega)$$

holding with high probability  $\mathbb{P}$ , i.e., with respect to the distribution of the stochastic process  $\mathbf{S}$  generating the features. We indicate throughout with  $\pi[\cdot]$  the expectation with respect to the reference distribution  $\pi$ .

For all  $m \geq 1$ , and  $\omega \in \Omega$  such that  $\rho(\cdot, \omega)$  is absolutely continuous with respect to the reference

Symbol	Meaning
$\rho$	Generalized posterior distribution
$\pi$	Reference distribution
$h_\theta$	Feed Forward Neural Network
$Lip(\cdot)$	Lipschitz constant
$R(\cdot)$	Population risk
$r(\cdot)$	Empirical risk
$KL$	Kullback-Leibler divergence
$\mathcal{X}^2$	Chi-square divergence
$\epsilon$	Accuracy level
$m$	Length of the training set
$\delta$	Confidence level
$D$	Dimension of the input
$a$	Temporal distance between $\mathbf{Y}_i$ and $\mathbf{Y}_{i+1}$ (parameter)
$p$	Past time steps used to design $\mathbf{X}_i$ (hyperparameter)
$\theta_{lex(a-p)}$	$\theta$ -lex coefficient of $\mathbf{Z}$

Table 1: summary of all parameters, hyperparameters, and symbols appearing in the inequality (9)

distribution  $\pi$ , the following inequality holds with probability  $\mathbb{P}$  at least  $1 - 2\delta$  for  $\delta \in (0, 1)$ :

$$\rho[R(h_\theta)] \leq \rho[r(h_\theta)] + \frac{KL(\rho, \pi) + \log\left(\frac{1}{\delta}\right)}{\sqrt{m}} + \frac{\epsilon^2}{2\sqrt{m}} + \left(\frac{\epsilon}{\delta}\pi[2(Lip(h_\theta)D + 1)\theta_{lex(a-p)}](\mathcal{X}^2(\rho, \pi) + 1)\right)^{\frac{1}{2}}. \quad (9)$$

In the inequality,  $\theta_{lex(a-p)}$  is a  $\theta$ -lex coefficient of the data generating process  $\mathbf{Z}$  (an STOU process in our assumptions) and  $Lip(h_\theta)$  refers to the Lipschitz coefficient of the feed-forward neural network  $h_\theta$  for a given realization  $\theta$  of the parameters. The symbols  $KL$  and  $\mathcal{X}^2$  stand for the *Kullback-Leibler* and *Chi-square* divergence between two probability measures, respectively. A proof of the inequality (9) can be found in [9]. We report in Table 1 a summary of all parameters, hyperparameters, and symbols appearing in the inequality (9) for clarity.

We could then select a generalized posterior distribution  $\rho$  that minimizes the right-hand side of the inequality (9). The generalized posterior selected in this way achieves the best possible generalization performance on data generated by  $\mathbf{S}$ , since the PAC-Bayesian bound certifies that the average generalization gap is minimal with high probability. If, for example,  $\delta = 0.025$ , the algorithm is expected to generalize well, i.e., it has a low expected generalization gap with probability 95%. Note that, given an accuracy level  $\epsilon$ , the bound of the expected generalization gap in (9) doesn't have to overcome this threshold to give a generalization guarantee. We call such bounds *non-vacuous*. The ideal optimization routine will then be to select, for a given observed data set (which in our notations corresponds to one  $\omega \in \Omega$ ), a generalized posterior distribution  $\rho$  belonging to the set of all probability measures defined on  $(\mathbb{R}^d, \mathcal{B}(\mathbb{R}^d))$  which minimizes the following target function:

$$\rho[r(h_\theta)] + \frac{KL(\rho, \pi) + \log\left(\frac{1}{\delta}\right)}{\sqrt{m}} + \left(\frac{\epsilon}{\delta}\pi[2(Lip(h_\theta)D + 1)\theta_{lex(a-p)}](\mathcal{X}^2(\rho, \pi) + 1)\right)^{\frac{1}{2}}. \quad (10)$$

Note that the addend  $\frac{\epsilon^2}{2\sqrt{m}}$  appearing in the inequality (9) is not included because it is a constant factor

and does not depend on  $\theta$ . A theoretical solution for (10) is an open problem. We then turn to a numerical optimization. The problem with optimizing (10) with respect to  $\rho$  in the space of all probability measures on  $(\mathbb{R}^d, \mathcal{B}(\mathbb{R}^d))$  lies in the simultaneous presence of the *KL* and *Chi-square* divergence in the bound. Especially, optimizing the *Chi-square* leads to several numerical instabilities [15]. Therefore, we typically approximate it instead of basing an optimization routine on its original definition, see [12, 35] for some exemplary solutions. In this work, we *linearize* the *Chi-square* divergence using a Taylor approximation [31], that is we approximate  $\chi^2(\rho, \pi) \simeq 2KL(\rho, \pi)$ . Next, we choose the parameter  $a$  in the embedding such that for  $\delta = 0.025$

$$\theta_{\text{lex}}(a - p) \sim \exp(-\lambda(a - p)) \leq \frac{\delta}{2m\epsilon}. \quad (11)$$

In conclusion, training in our methodology means selecting a generalized posterior distribution  $\rho \in \{\mathcal{N}(\mu, \text{diag}(\kappa)) \text{ for } \mu \in \mathbb{R}^d \text{ and } \kappa \in \mathbb{R}_+^d\}$  which minimizes the target function

$$\rho[r(h_\theta)] + \frac{KL(\rho, \pi) + [(2KL(\rho, \pi) + 1)(\pi[\text{Lip}(h_\theta)]D + 1)]^{1/2}}{\sqrt{m}}, \quad (12)$$

with  $\pi \sim N(0, sI_d)$ ,  $s \in \mathbb{R}_+$ , being a multivariate Gaussian distribution with diagonal covariance matrix. The generalized posterior distribution obtained by minimizing the target function (12) loses its interpretation as the right-hand side of a PAC-Bayesian bound. However, our experiments in Section 4 show that we typically obtain an approximation  $\rho^*$  of the minimum to which corresponds, for our choice of the parameter  $a$ , a non-vacuous PAC Bayesian bound holding with probability of at least 95%. We give in Algorithm 2 a description of the training routine. Note that, in general, the algorithm can use batch learning (where the batches are taken in chronological order) and epochs.

---

**Algorithm 2** MMAF-guided learning training algorithm for stochastic feed-forward neural networks for a spatial position  $x^*$ .

---

**Input:**  $S_m = \{(X_i, Y_i)\}_{i=1}^m$  Training data set.  
 $m'$  Batch size.  
 $N'$  Number of batches.  
 $\epsilon, \eta \in \mathbb{R}_+$  Accuracy level, Adam learning rate.  
 $\pi \sim \mathcal{N}(0, sI_d)$  Reference distribution,  $s \in \mathbb{R}_+$ .  
 $h_\theta$  Feed-forward neural network architecture,  $\theta \in \mathbb{R}^d$ .  
 $\rho^0 \sim \mathcal{N}(\mu^0, \text{diag}(\kappa^0))$  Initialization of the generalized posterior distribution with  $\mu^0 := 0 \in \mathbb{R}^d, \kappa^0 \in \mathbb{R}_+^d$ .

**for**  $\iota = 0, \dots, N' - 1$  **do:**

1. Estimate  $Lip(h_\theta)$  using the upper bound

$$Lip(h_\theta) \leq \prod_{i=1}^{\ell+1} \|W^{(i)}\|_2 \quad (13)$$

2. Compute the Monte Carlo estimator of  $\pi[Lip(h_\theta)]$  using the bound (13):

$$\pi[Lip(h_\theta)] \simeq \frac{1}{1000} \sum_{j=1}^{1000} \prod_{i=1}^{\ell+1} \|W_j^{(i)}\|_2,$$

where  $\theta^j = (W_j^{(1)}, \dots, W_j^{(\ell)}, W_j^{(\ell+1)}, b_j^{(1)}, \dots, b_j^{(\ell)})$  is drawn from  $\pi$  for  $j = 1, \dots, 1000$ .

3. Compute  $\nabla \rho^\iota[r(h_\theta)]$  employing pathwise gradient estimator:

$$\nabla_{(\mu^\iota, \kappa^\iota)} \rho^\iota[r(h_\theta)] \simeq \nabla r(h_{\theta^\iota}), \quad \theta^\iota \text{ single draw from } \rho^\iota, \quad (14)$$

where

$$r(h_{\theta^\iota}) = \frac{1}{m'} \sum_{j \in \mathcal{J}_\iota} L^\epsilon(h_{\theta^\iota}(X_j), Y_j),$$

where  $\mathcal{J}_\iota = \{\iota m' \dots, (\iota + 1)m'\}$  is the  $\iota$ -th batch.

4. Compute

$$KL(\rho^\iota, \pi) = \frac{1}{2} \sum_{i=1}^d \left( \log \left( \frac{s}{\kappa_i^\iota} \right) - 1 + \frac{\kappa_i^\iota}{s} + \frac{(\mu_i^\iota)^2}{s} \right)$$

5. Compute

$$\nabla_{(\mu^\iota, \kappa^\iota)} \left( \frac{KL(\rho^\iota, \pi) + ((2KL(\rho^\iota, \pi) + 1) \left( \frac{D}{1000} \sum_{j=1}^{1000} \prod_{i=1}^{\ell+1} \|W_j^{(i)}\|_2 + 1 \right))^{1/2}}{\sqrt{m}} \right) \quad (15)$$

6. Update  $\rho^{\iota+1}$  using Adam update rule with  $f(\theta^\iota) := (14) + (15)$  and learning rate  $\eta$ .

**end for**

**Output:**  $\rho^*$

---

### 3.2 Causal Forecast and Inference

Let  $X_i$  be an input belonging to the validation or test data set related to the spatial position  $x^*$ , i.e.,  $X_i = (Z_{i_1}(x_1), \dots, Z_{i_D}(x_D))^\top$  for  $(i_s, x_s) \in I(t_0 + ia, x^*)$  and  $i = m + 1, \dots, \lfloor \frac{N}{a} \rfloor$ . Then, following the definition given in (5), the input vector  $X_i$  can be used to forecast the values of the field  $\mathbf{Z}$  which corresponds to the spatial-time positions

$$A(X_i)^+ := \{(t, s) \in \bigcap_{s=1}^D A_{i_s}(x_s)^+\}$$

Note that the spatial-time position  $(t_0 + ia, x^*)$  belongs to  $A(X_i)^+$  and can then be forecasted starting from the input  $X_i$ , see Figure 2.

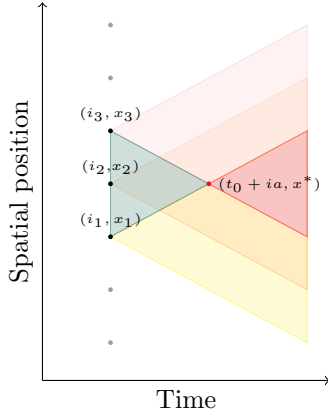


Figure 2: The black dots indicate the spatial-temporal index grid  $\mathbb{R} \times \mathbb{R}$ , corresponding to an input feature  $X_i = (Z_{i_1}(x_1), Z_{i_2}(x_2), Z_{i_3}(x_3))$  for  $(i_s, x_s) \in I(t_0 + ia, x^*)$ . The pink area identifies the future cone of influence related to the spatial-time position  $(i_1, x_1)$ , the orange area the future cone of influence from  $(i_2, x_2)$ , and the yellow one the future cone of influence from  $(i_3, x_3)$ . All three spatio-temporal positions together influence the future realizations of the field at the spatio-temporal points in the red area, which is a subset of  $\mathbb{R} \times \mathbb{R}$ .

In MMAF-guided learning, we forecast the values of the field  $\mathbf{Z}$  at the time points  $t_0 + ia$  for  $i = m + 1, \dots, \lfloor \frac{N}{a} \rfloor$  at the spatial position  $x^*$ . Other forecasting schemes can be investigated based on the input features' ability to predict future values of the data-generating process. For example, in [9] the authors investigate a scheme where the forecasts correspond to one-step ahead with respect to the information contained in the training data set. The latter scheme also has a causal interpretation, and it can be extended to multiple time steps into the future. We leave the analysis of such forecasting schemes to future applications of MMAF-guided learning.

In Section 4, we employ a training data set

$$\mathcal{T} = (S_m^1, S_m^2, \dots, S_m^R)$$

corresponding to  $R$  different spatial positions in a raster. At the end of the training step (parallelized with respect to each spatial position), we obtain the set of generalized posterior distributions  $\{\rho^{*,1}, \rho^{*,2}, \dots, \rho^{*,R}\}$ . The latter are used in inference mode to compute ensemble forecasts for each spatial position at times  $t = t_0 + ia$  for  $i = m + 1, \dots, \lfloor \frac{N}{a} \rfloor$ , where  $\lfloor \frac{N}{a} \rfloor$  represents the furthest time horizon that is allowed given

an observed raster dataset of length  $N$ . In our experiments, we call  $H \in \{0, \dots, \lfloor \frac{N}{a} \rfloor - i\}$  the terminal horizon for which forecasts are desired starting from an observation at time  $t = t_0 + ia$ . We describe below the Algorithm 3 which generates ensemble forecasts (in a given spatial position  $r \in \{1, \dots, R\}$ ) with  $J$  members across  $H$ -time horizons.

---

**Algorithm 3** Inference step: ensemble forecasts generation across multiple time horizons for a single spatial position  $r$ .

---

**Input:**  $\rho^{*,r}$  Generalized posterior distribution on  $(\mathbb{R}^d, \mathcal{B}(\mathbb{R}^d))$   
 $X_i$  Input belonging to the validation or test set  
 $H$  Terminal time horizon  
 $h_\theta$  Feed-forward neural network architecture,  $\theta \in \mathbb{R}^d$ .  
 $J$  Number of ensemble members.

**for**  $j = 1 \dots J$  **do:**

1. Draw a sample  $\theta^j$  from  $\rho^{*,r}$ .
2. Compute  $(h_{\theta^j}(X_{i+h}), \dots, h_{\theta^j}(X_{i+h}))_{h=0}^H$ , the  $j$ -th member of the ensembles.

**end for**

**Output:**  $[(h_{\theta^1}(X_{i+h}), \dots, h_{\theta^J}(X_{i+h}))_{h=0}^H]$

---

We claim that the ensemble members for a fixed spatial position and horizon  $h \in \{0, \dots, \lfloor \frac{N}{a} \rfloor - i\}$  for  $i = m + 1, \dots, \lfloor \frac{N}{a} \rfloor$ , are samples from a distribution that approximates  $\mathbb{P}(\mathbf{Y}_{i+h} | \mathbf{X}_{i+h} = X_{i+h})$ , i.e., the *conditional predictive distribution of the data* in our setup which is unknown and, in general, not of Gaussian type. We test this claim in the next section by employing the CRPS score [16], a probabilistic metric that assesses the consistency between the ensemble members' distributions and the observed value.

## 4 Experiments

### 4.1 Data set and Training set-ups

We employ three datasets in our experiments on stochastic feed-forward neural networks. Two are synthetic datasets sampled from an STOU process with a Gaussian and a normal inverse Gaussian distributed Lévy basis, generated using the diamond grid algorithm introduced in [28]. We refer to the synthetic datasets as GAU and NIG throughout, both of which consist of raster datasets with 10 spatial positions, 8 of which are used in the inference step, and  $N = 10^6$  temporal records. The last one is a real data set called *Outgoing Longwave Radiation Anomalies* (OLR) from the *NCEP CPC pentad OLR anomalies*, provided by the International Research Institute for Climate and Society [18]. The OLR dataset contains 144 spatial components, corresponding to a longitude east in degrees of  $0, 2.5, \dots, 375.5$ , whereas the temporal component consists of sets of 5 days starting from October 13 – 18th 1974 until December 27 – 31st 2022 for a total of  $N = 3520$  temporal records. We use as a variable the 5 days average outgoing longwave radiation anomalies averaged over the latitudes 5 degrees south to 5 degrees north, measured

in Watts per square meter. Negative anomalies imply increased cloudiness and an enhanced likelihood of precipitation, while positive anomalies imply decreased cloudiness and a lower chance of precipitation. Eight spatial locations between latitudes north in degrees  $9, \dots, 29$  are used in the inference step. For all data sets, we set  $t_0 = 0$  throughout.

First, we need to determine the embedding for each spatial position of interest. This is done by estimating the values of the *mean reverting parameter*  $A$ , the *speed of information propagation*  $c$ , and the decay rate  $\lambda$  of the  $\theta$ -lex coefficients of  $\mathbf{Z}$ , following the estimation procedure in Appendix A. The estimations of such values are listed in Table 2 for all three datasets. Such estimations allow us to learn the dependence and causal structure of the data under our modeling assumption. We then select the hyperparameters  $p$  and  $\epsilon$  following the theoretical framework of [9], which provides the necessary insights to tune them accordingly: that is,  $p$  is chosen equal to 1 for ease of computation and  $\epsilon = 3$ . We then select the parameter  $a$  according to rule (11), yielding  $a = 8$  for the GAU and NIG data sets and  $a = 64$  for the OLR dataset. All obtained features are then partitioned along the temporal dimension following the characterization given in Section 2.2 for the training, validation, and test data sets. The length of the training data set is  $m = 124899$  for the GAU and NIG frameworks, whereas  $m = 36$  for the OLR data set. Moreover, the validation set consists of a single example, and the test sets contain 100 and 18 examples for GAU/NIG and OLR frameworks, respectively.

We refer to each feed-forward architecture using the symbol  $w^\ell$ , where we assume that the inner layers have the same width, i.e.,  $w := n_1 = \dots = n_\ell$  following the notations of Section 3.1 and  $\ell$  is the number of the hidden layers. In our study, we consider six networks, denoted by  $10^2$ ,  $10^5$ ,  $30^2$ ,  $100^2$ ,  $300^2$ , and  $800^3$ . The training routine is performed in parallel across 8 spatial coordinates. We perform batch learning for the GAU and NIG datasets with  $m' = 1000$  and run the algorithm for 30 epochs. In the case of the OLR data set, we use the optimization routine without batch learning and run the algorithm for 3000 epochs. The stopping rule of our training is based on the convergence study in Appendix C.

Data Set	$A^*$	$c^*$	$\lambda^*$	m	a
GAU	3.851	1.013	1.896	124899	8
NIG	3.869	0.998	1.938	124899	8
OLR	0.697	4.853	0.144	36	64

Table 2: Estimation of parameters  $A$ ,  $c$ ,  $\lambda$ , size of the training data set  $m$ , and chosen parameter  $a$  following rule (11).

In our experiments, we initialize the mean of the reference and posterior distributions to the zero vector, and initialize the covariance matrix of the posterior distribution to  $\frac{1}{4}I_d$ . The covariance matrix of the reference distribution is *validated* following the procedure described in Section 4.3.

## 4.2 Evaluation Metrics

Starting from a time  $ia$  for  $i = m + 1, \dots, \lfloor \frac{N}{a} \rfloor$ , we can determine ensemble forecasts for multiple-time horizons. Let  $H \in \{0, \dots, \lfloor \frac{N}{a} \rfloor - i\}$  the terminal horizon in our experiments. We then indicate the related ensemble forecasts (in a given spatial position) with  $J$  members across  $H$ -time horizons with  $[(h_{\theta^1}(X_{i+h}), \dots, h_{\theta^J}(X_{i+h}))]_{h=0}^H$ , and with  $Y_{i+h}$  for  $h = 0, \dots, H$  the observed values at the time  $(i+h)a$  which we use in the evaluation of our metrics. In our evaluations, we consider two of them.

The first is the *Root Mean Squared Error* (RMSE), a deterministic metric, defined as

$$RMSE = \sqrt{\frac{1}{H} \sum_{h=0}^H \frac{1}{J} \sum_{j=1}^J (h_{\theta^j}(X_{i+h}) - Y_{i+h})^2}$$

The second metric we employ is the *Continuous Ranked Probability Score* (CRPS), a probabilistic metric used to assess the calibration and sharpness of ensemble forecasts, as described in [17] and [16], and it is specified in terms of the cumulative distribution function (cdf) related to the predictive distribution  $\mathbb{P}(\mathbf{Y}_{i+h} | \mathbf{X}_{i+h} = X_{i+h})$  for a given time horizon  $h$ . It allows us to evaluate if the ensemble forecast  $(h_{\theta^1}(X_{i+h}), \dots, h_{\theta^J}(X_{i+h}))$  is consistent with respect to the observed value  $Y_{i+h}$ , and it is defined as

$$CRPS(\mathbb{P}(\mathbf{Y}_{i+h} | \mathbf{X}_{i+h} = X_{i+h}), Y_{i+h}) = \mathbb{E}[\mathbf{Y} - Y_{i+h}] - \frac{1}{2} \mathbb{E}[\mathbf{Y} - \mathbf{Y}'], \quad (16)$$

where the random variables  $\mathbf{Y}$  and  $\mathbf{Y}'$  are independent random variables distributed with respect to the (conditional) predictive distribution  $\mathbb{P}(\mathbf{Y}_{i+h} | \mathbf{X}_{i+h} = X_{i+h})$ . In our framework, it is not possible to have access to its cdf, so we compute the empirical counterpart of (16) using the ensemble forecast  $(h_{\theta^1}(X_{i+h}), \dots, h_{\theta^J}(X_{i+h}))$ . Note that all values reported in our tables below are averaged across the number of horizons and the spatial positions considered.

### 4.3 Validation of the reference distribution

We set up the following grid for the selection of the covariance matrix of the reference distribution,

$$\{s^{-1}I_d : s \in \{10, 30, 50, 70, 90, 110, 130, 150, 170, 190, 210\}\}.$$

We then validate the choice of the covariance matrix with respect to the parameter  $s$  by minimizing the average CRPS score computed on the validation set. To the best of our knowledge, this is the first workflow where a CRPS score is used to validate the selection of a reference distribution. Several alternative strategies exist for choosing a reference distribution in PAC-Bayesian learning, as discussed, for example, in [3, 13]. However, such strategies have been mostly tested on random samples (i.e., independent and identically distributed data). We demonstrate in our experiments that the validation strategy above enables us to generate *ensemble forecasts* for the test set with CRPS scores of the same order of magnitude as those observed in validation. We refer to our forecasts to *remain calibrated across multiple time horizons* when the latter happens.

We can also draw a parallel between a well-known post-processing procedure used in weather forecasting, the EMOS [17], and our validation methodology. In the former, a minimum CRPS estimation (that makes use of observed data and ensemble forecasts produced by *numerical weather forecast models*) is used to produce calibrated ensemble forecasts in a given spatial-time position, whereas in the latter, we use CRPS minimization to select a prior distribution, which gives us a calibrated ensemble forecast on the validation set.

Table 3: Description of the architectures used in the experiments

Model	Architecture	Param.	Model	Architecture	Param.
SFFN	$[10^2]$	$\sim 10^2$	ConvLSTM	$150(k \times 1)-1(k \times k)$	$\sim 10^4$
SFFN	$[10^5]$	$\sim 5 \cdot 10^2$	ConvGRU	$2((k \times 1)-1(k \times k))$	$\sim 10^2$
SFFN	$[30^2]$	$\sim 10^3$	ConvGRU	$10(k \times 1)-1(k \times k)$	$\sim 5 \cdot 10^2$
SFFN	$[100^2]$	$\sim 10^4$	ConvGRU	$18(k \times 1)-1(k \times k)$	$\sim 10^3$
SFFN	$[300^2]$	$\sim 10^5$	ConvGRU	$180(k \times 1)-1(k \times k)$	$\sim 10^4$
SFFN	$[800^3]$	$\sim 10^6$	DiffSTG	$(T_h, T_f)-1$	$\sim 10^3$
ConvLSTM	$2(k \times 1)-1(k \times k)$	$\sim 10^2$	DiffSTG	$(T_h, T_f)-4$	$\sim 10^4$
ConvLSTM	$8(k \times 1)-1(k \times k)$	$\sim 5 \cdot 10^2$	DiffSTG	$(T_h, T_f)-11$	$\sim 10^5$
ConvLSTM	$15(k \times 1)-1(k \times k)$	$\sim 10^3$	DiffSTG	$(T_h, T_f)-40$	$\sim 10^6$

$\ell(k \times k)$ :  $\ell$  is the number of hidden layers and  $k$  refers to the kernel size.

$(T_h, T_f)-\ell$ : following [36],  $T_h$  and  $T_f$  represent the number of historical and future graph feature states, respectively; instead,  $\ell$  is the number of hidden layers in the UGnet.

$[w^\ell]$ :  $\ell$  is the number of hidden layers of the feed-forward architecture, and  $w$  is the width of each hidden layer.

#### 4.4 Baseline Models

We compare the performance of stochastic feed-forward neural networks trained using MMAF-guided learning (SFFN) in the following section against several baseline models used in probabilistic forecasting. We describe them briefly in this section.

- **ConvLSTM** is an auto-regressive model that combines different long short-term memory (LSTM) modules, and a recurrent neural network (RNN) module. These elements are combined together with convolution layers and a Gaussian head to produce a multivariate (Gaussian distributed) ensemble forecast output, see [34, 22] for a detailed description of the architecture.
- **ConvGRU** is an auto-regressive model that combines different gate recurrent units (GRU) with operations of convolution, followed by a Gaussian head, in order to generate a (Gaussian distributed) ensemble forecast output, see [25] for further details.
- **DiffSTG** is a non-autoregressive diffusion model for spatio-temporal graphs forecasting that makes use of a denoising UGnet network as described in detail in [36].

The baselines are defined by considering an increasing number of hidden layers, as reported in Table 3. To ensure a fair comparison across methodologies on the same time horizons, the number of past features used to generate forecasts is fixed to  $a$  for both the ConvLSTM and ConvGRU models. The kernel size  $k = 2pc + 1$  through all the simulations, where  $c = 1$  for the GAU and the NIG datasets,  $c = 4$  for the OLR datasets, and  $p = 1$ . The DiffSTG model is configured to use  $T_h = p$  historical graph feature states to predict a single graph feature state, i.e.,  $T_f = 1$ , where  $p$  is the hyperparameter reported in Table 1.

## 5 Results and Discussions

In this section, we present the results for the various experiments discussed in the previous sections. The source Python code is available in the following Github repository. The experiments were run on a machine with access to 256GB RAM, 48 GB NVIDIA A40, and 2 AMD EPYC 7313 16-Core Processors.

## 5.1 MMAF-guided learning applied to stochastic-feed forward neural networks

We present in Table 4, several aspects of the training, validation, and testing for the stochastic neural networks introduced in Section 4.1. In the column **Training**, we find the value of the target function (12) and of the right-hand side of the bound (9) (for a confidence parameter  $\delta = 0.025$ ) computed with respect to the generalized posterior distributions obtained at the end of the training routine. These results indicate that Algorithm 2 mostly selects posterior distributions at each spatial position that have low average generalization gaps with a probability of at least 95%. We obtain comparable performance across datasets and architectures, except for the architecture  $800^3$ , which is the only one for which we obtain a vacuous PAC Bayesian bound, indicating that the network overparameterization has a toll on the generalization performance of the posterior distribution.

In the columns related to the **Validation** of our methodology, we report the value of the reference distribution selected in our methodology, along with the corresponding CRPS and RMSE. Finally, in the columns related to the **Test**, we find the value of the CRPS and RMSE averaged with respect to the time horizons. We note that the CRPS values are of the same order of magnitude and within the same range as those observed in the validation set, indicating that the ensemble forecast remains calibrated in time. On the other hand, the RMSE increases during evaluation on the test set, indicating that error accumulation occurs across time horizons.

Dataset	Architecture	Training		Validation			Test		
		Target (12)	PAC bound (9)	$\pi$	CRPS	RMSE	Horizons	CRPS	RMSE
GAU	$[10^2]$	0.1131	0.487	$N(0, 1/30)$	0.0533	0.0146	100	0.0590	0.0158
	$[10^5]$	0.1120	0.4885	$N(0, 1/30)$	0.0537	0.0147	100	0.0592	0.0157
	$[30^2]$	0.1198	0.4970	$N(0, 1/50)$	0.0515	0.0157	100	0.0601	0.0172
	$[100^2]$	0.1623	0.5317	$N(0, 1/90)$	0.0546	0.0184	100	0.0588	0.0188
	$[300^2]$	0.3538	0.8122	$N(0, 1/150)$	0.0499	0.0206	100	0.0617	0.0230
	$[800^3]$	4.2854	$2.4 \times 10^{13}$	$N(0, 1/210)$	0.0771	0.0722	100	0.0879	0.0787
NIG	$[10^2]$	0.0308	0.4061	$N(0, 1/210)$	0.0042	0.0002	100	0.0220	0.0018
	$[10^5]$	0.0313	0.4064	$N(0, 1/210)$	0.0042	0.0002	100	0.0216	0.0018
	$[30^2]$	0.0366	0.4111	$N(0, 1/210)$	0.0054	0.0004	100	0.0208	0.0020
	$[100^2]$	0.0703	0.4402	$N(0, 1/210)$	0.0095	0.0015	100	0.0225	0.0032
	$[300^2]$	0.2778	0.7767	$N(0, 1/210)$	0.0183	0.0059	100	0.0302	0.0077
	$[800^3]$	4.9759	$1.92 \times 10^{16}$	$N(0, 1/210)$	0.0731	0.0681	100	0.0775	0.0710
OLR	$[10^2]$	0.5063	2.4843	$N(0, 1/30)$	0.2688	0.1356	18	0.443	0.3443
	$[10^5]$	0.5083	2.4853	$N(0, 1/30)$	0.2748	0.1326	18	0.4481	0.3436
	$[30^2]$	0.5527	2.5312	$N(0, 1/30)$	0.2245	0.1769	18	0.3943	0.3815
	$[100^2]$	0.7461	2.6548	$N(0, 1/50)$	0.2049	0.2238	18	0.3714	0.4284
	$[300^2]$	1.4485	3.5668	$N(0, 1/90)$	0.205	0.2707	18	0.3580	0.4609
	$[800^3]$	12.30	232.81	$N(0, 1/210)$	0.1357	0.1725	18	0.3641	0.4792

Table 4: Performance of MMAF-guided learning in training, validation, and test for the GAU, NIG, and OLR data sets. The value of the target function and the PAC bound in training are averaged across the spatial positions considered in the study; the CRPS is averaged with respect to the time horizons and spatial positions; and the RMSE is averaged with respect to the spatial positions.

## 5.2 Comparison of model results

We compare MMAF-guided learning applied to stochastic feed-forward neural networks with the baseline ConvLSTM, ConvGRU, and DiffSTG models described in Section 4.4.

First, it is important to note that different training datasets are used for the ConvLSTM, ConvGRU, and DiffSTG models than in the stochastic feed-forward neural network setup. The reason is that we do not use the optimization routine described in Algorithm 2. Therefore, the models use the entire raster dataset as training data. For the GAU and NIG, this corresponds to  $m = 999192$ , and for the OLR data set, to  $m = 2304$ . The training data set used in MMAF-guided learning is then significantly smaller than that used for the baseline models. Regarding the time horizons considered in our forecasting tasks, we use those corresponding to the test data set for the stochastic feed-forward neural network described in Section 2.2, to maintain consistency in the forecast evaluation.

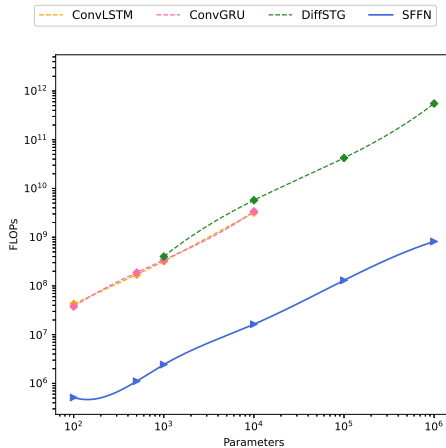


Figure 3: Comparison of the computational cost in FLOPs of a training iteration for an ensemble of 8 stochastic feed-forward neural networks against the baseline models in the case of the OLR data set.

Figure 3 shows the number of FLOPs, i.e., floating point operations per second, used during a training iteration for the stochastic feed-forward neural networks and the baseline models used in the case of the OLR dataset. Figure 3 shows that the training phase in MMAF-guided learning is more computationally efficient than in the other setups. The same pattern is observed across different architectures for the GAU and NIG data sets.

We then analyze the quality of the probabilistic forecasts obtained for all the architectures described in Table 3 for the datasets GAU, NIG and OLR with respect to the CRPS and the RMSE score (averaged across the spatial positions and time horizons analyzed). We report the results in Figure 4, and a list of the models with the lowest CRPS and RMSE score in Table 5.

In terms of CRPS score, the DiffSTG model setup shows the best forecasting performance across the datasets, with performance improving as the number of parameters increases (i.e., for the deepest architecture presented in Table 3). Stochastic feed-forward neural networks, within the GAU and NIG framework, achieve better forecasting performance with simpler architectures than with deeper ones. For the OLR dataset, we observe that overparameterization improves forecasting performance, matching the performance of the deepest networks we experiment with and being comparable to that of the diffusion setup. The difference in performance may be due to differences in the number of features available for

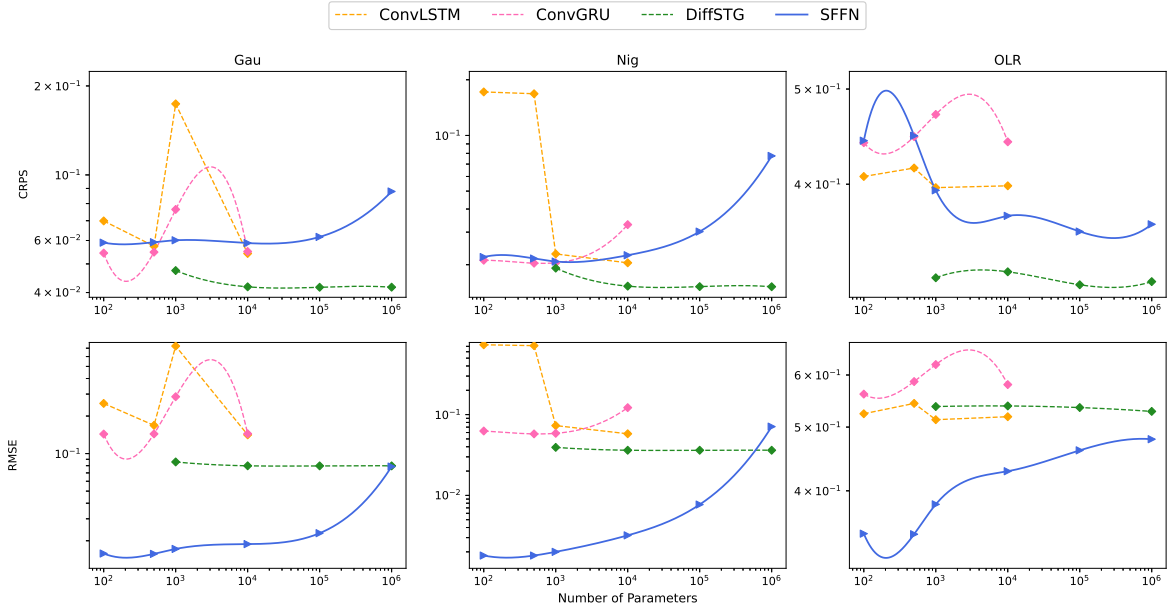


Figure 4: Comparison between the ensemble of stochastic feed-forward neural networks and the baseline models on the test set for the datasets GAU, NIG, and OLR with respect to the CRPS and RMSE score and the number of model parameters.

Model	GAU			NIG			OLR		
	Architecture	CRPS	RMSE	Architecture	CRPS	RMSE	Architecture	CRPS	RMSE
SFFN	[100 <sup>2</sup> ]	0.0588	0.0188	[30 <sup>2</sup> ]	0.0208	0.0020	[300 <sup>2</sup> ]	0.3580	0.4609
ConvLSTM	150(3 × 1)- 1(3 × 3)	0.0542	0.1414	8(3 × 1)- 1(3 × 3)	0.1681	0.7140	15(9 × 1)- 1(9 × 9)	0.3968	0.5131
ConvGRU	2(3 × 1)- 1(3 × 3)	0.0544	0.1435	10(3 × 1)- 1(3 × 3)	0.0204	0.0577	2(9 × 1)- 1(9 × 9)	0.4409	0.5612
DiffSTG	(1,1)-40	0.0417	0.0797	(1,1)-11	0.0152	0.0362	(1,1)-40	0.3183	0.5282

Table 5: Models with lowest CRPS and RMSE score across the architecture described in Table 3

training or to the actual dependence structure of the data, which is unknown to us in the case of the OLR dataset and may have a strong impact on the different behavior of the forecast with respect to a Gaussian and heavy-tailed (driven by a NIG distribution) framework as in the case of the GAU and NIG data. In most of the setups, we have found that our methodology outperforms the ConvLSTM and ConvGRU frameworks. With respect to the RMSE, we also observe that stochastic feed-forward neural networks can outperform the diffusion setup, showing that, as the time horizons grow, our methodology accumulates forecast errors at a lower rate. Moreover, with respect to this metric, overparameterization does not show a positive effect.

Next, we present a study that focuses on a more careful comparison between the diffusion and the stochastic feed-forward setup. In Figure 5, the DiffSTG discussed in the previous paragraph, together with the *DiffSTG embedded* set-up, which uses in its training a number of data that corresponds to the raster selected by the embedding used in MMAF-guided learning. We indicate this latter setup with the light green curve. With this experiment, we want to check whether the diffusion setup maintains its forecasting

performance when trained on the same data embedding used in MMAF-guided learning. For the GAU and NIG dataset we observe that the diffusion model performs better on the CRPS score when trained on more data and with deeper architectural choices. On the other hand, the *DiffSTG embedded* setup has a comparable CRPS score to that of stochastic feed-forward neural networks with fewer than  $10^4$  parameters. Regarding the OLR data set, the *DiffSTG embedded* setup outperforms the standard DiffSTG setup with respect to the CRPS score, suggesting that the embedding strategy used in MMAF-guided learning can be used as a standalone component in the design of a probabilistic forecast model. Regarding the RMSE, we observe that stochastic feed-forward neural networks generally yield lower values than the diffusion setups, indicating that the methodology presented in the paper accumulates slower prediction error across forecasting horizons.

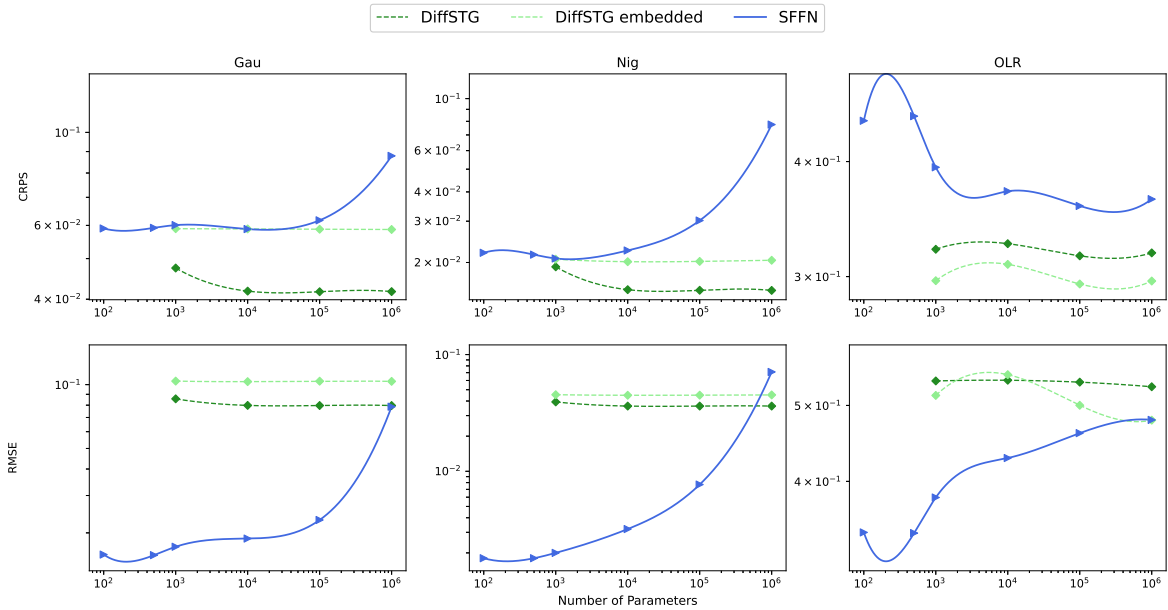


Figure 5: Comparison between the ensemble of stochastic feed-forward neural networks and different diffusion frameworks on the test set for the datasets GAU, NIG, and OLR with respect to the CRPS and RMSE score and the number of model parameters.

Figure 6 visualizes the prediction intervals (via empirical quantile ranges of the ensemble forecasts) at various confidence levels, corresponding to increasing probability levels from 10% to 95% and a pooled PIT histogram across 100 time horizons for the 5th spatial position in the case of the GAU data set determined for the models in Table 5. Moreover, given that in the training of the stochastic feed-forward neural networks, the value of the CRPS score changes slightly between the smallest model  $10^2$  and the one appearing in the Table 5, we also showcase such diagnostic plots to determine if using small feed-forward neural networks achieves comparable performance with the other models. As can be observed, the test data set lies within the prediction intervals and respects their nominal value across setups. Instead, we observe that the PIT histogram has the best behaviors for the SFNN and the DiffSTG models from Table 5, with a slight deterioration in the case of the smallest neural network  $10^2$ . Similar behavior is observed at every spatial position analyzed in the raster and also in the NIG and OLR frameworks. We can then conclude that the forecast obtained using stochastic feed-forward neural networks has comparable quality

to those determined within a diffusion framework, but at lower computational cost.

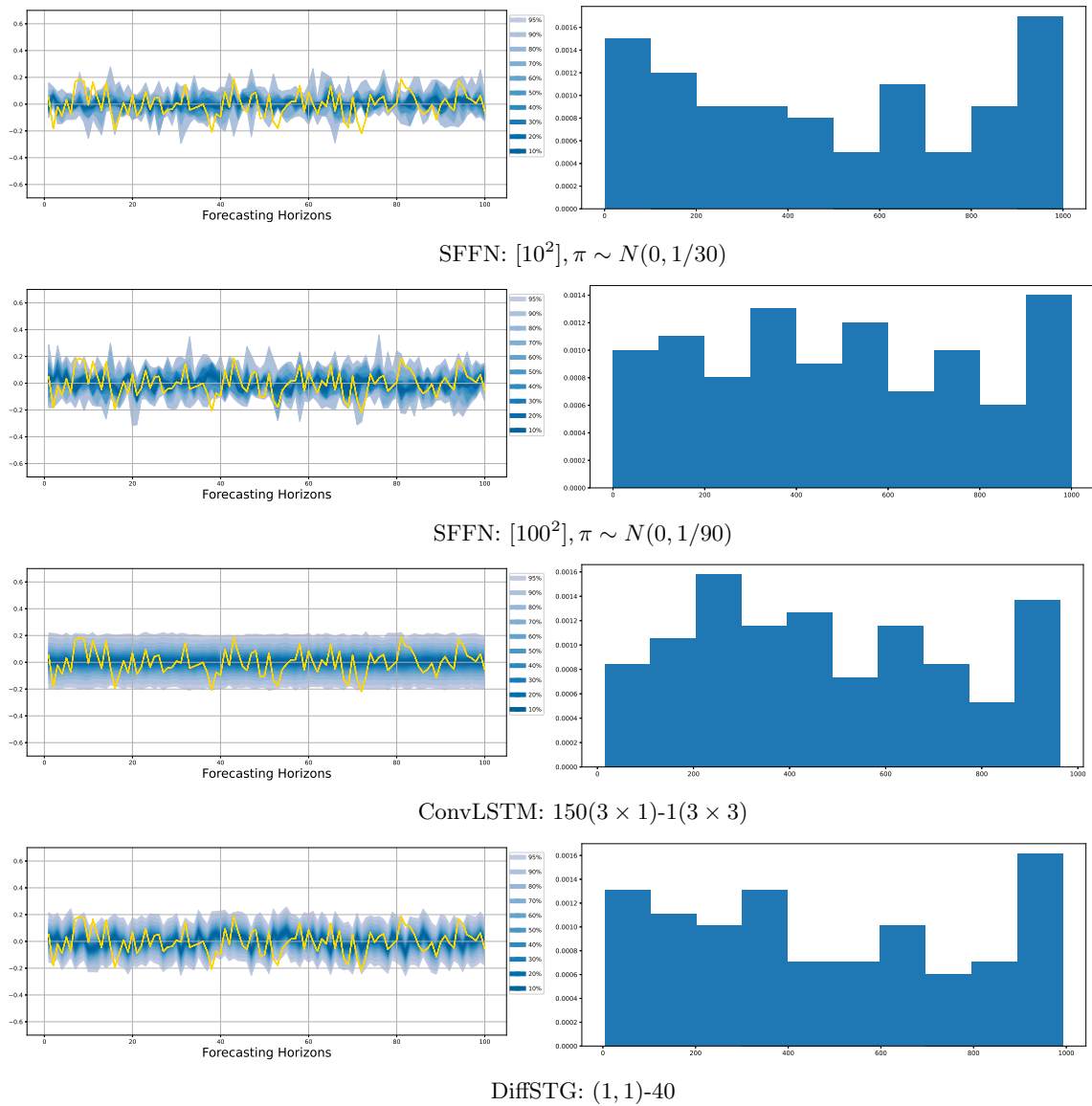


Figure 6: Comparison of ensemble forecasts (left) and their corresponding PIT histogram over time (right), generated using a stochastic feed-forward neural network, ConvLSTM, and DiffSTG respectively, across 100 horizons versus the GAU test dataset in gold (5th coordinate). The percentages in the legend indicate the quantile ranges of the ensemble forecasts.

## 6 Conclusions and future work

We present a novel methodology for dependence and causal structure estimation, feature extraction, and probabilistic forecasting of a raster dataset across multiple time horizons. Our methodology assumes that an STOU process generates the data. The latter is a special case of a class of fields called MMAF, which in turn belongs to the class of the Ambit fields [5]. The latter is a class of random fields that can be

employed to model a range of phenomena, from turbulent flows to energy market derivatives, and is, in general, applied to model non-stationary phenomena. Our probabilistic forecasting methodology has the potential to be applied to such a class of fields, once the embedding and feature learning from the data are modified to accommodate a non-stationary set-up. The latter is a promising direction for research and will be addressed in future work. Future directions of our work also investigate a feasible procedure for 3D raster datasets in the presence of power decaying autocorrelation functions in the data, and a PAC Bayesian bound for MMAF-generated data that allows us to consider unbounded loss functions and therefore defining a more versatile optimization routine for the training of ensemble of stochastic feed-forward neural networks, see [4] and [11], respectively.

## References

- [1] P. Alquier and B. Guedj. Simpler PAC-Bayesian bounds for hostile data. *Mach. Learn.*, 107 (5):887–902, 2018.
- [2] P. Alquier and O. Wintenberger. Model Selection for Weakly Dependent Time Series Forecasting. *Bernoulli*, 18 (3):883–913, 2012.
- [3] Pierre Alquier. User-friendly introduction to PAC-Bayes bounds. *Found. Trends Mach. Learn.*, 17(2):174–303, jan 2024.
- [4] L. Bardi, I. V. Curato, and L. Proietti. Probabilistic forecast for spatio-temporal ornstein-uhlenbeck processes. work in progress, 2026.
- [5] O. E. Barndorff-Nielsen, F. E. Benth, and A. E. D. Veraart. *Ambit Stochastics*. Springer, Cham, 2018.
- [6] N. D. Brenowitz, Y. Cohen, J. Pathak, A. Mahesh, B. Bonev, T. Kurth, s. R. Durran, P. Harrington, and M. S. Pritchard. A practical probabilistic benchmark for AI weather models. *Geophysical Research Letters*, 52:e2024GL113656, 2025.
- [7] O. Catoni. *Statistical Learning Theory and Stochastic Optimization*. Lecture notes in Mathematics, Springer, Berlin, 2004.
- [8] N. Cressie and C. K. Wikle. *Statistics for Spatio-Temporal Ddata*. John Wiley & Sons, Inc., Hoboken, New Jersey, 2011.
- [9] I. V. Curato, O. Furat, L. Proietti, and B. Ströh. Mixed moving average field guided learning for spatio-temporal data. *Electron. J. Stat.*, 19(1):519 – 592, 2025.
- [10] I. V. Curato, R. Stelzer, and B. Ströh. Central limit theorems for stationary random fields under weak dependence with application to ambit and mixed moving average fields. *Ann. Appl. Probab.*, 32:1814–1861, 2022.
- [11] I. V. Curato and J. Sternkopf. Mixed moving average field guided learning with unbounded losses. work in progress, 2026.

- [12] A. B. Dieng, D. Tran, R. Ranganath, J. Paisley, and D.M. Blei. Variational inference via  $\mathcal{X}$  upper bound minimization. In *Advances in Neural Information Processing Systems*, 2017.
- [13] G. K. Dziugaite and D. M. Roy. Computing Nonvacuous Generalization Bounds for Deep (stochastic) Neural Networks with Many More Parameters than Training Data. In *Proc. of the Conf. on Un. in Art. Int.*, 2017.
- [14] D. T. Frazier, C. Drovandi, and R. Kohn. Calibrated generalized bayesian inference. arXiv:2311.15485, 2024.
- [15] Tomas Geffner and Justin Domke. On the difficulty of unbiased alpha divergence minimization. In *Proceedings of the 36th International Conference on Machine Learning (ICML)*. PMLR, 2019.
- [16] T. Gneiting, F. Balabdaoui, and A. E. Raftery. Probabilistic forecasts, calibration and sharpness. *Journal of the Royal Statistical Society. Series B (Statistical Methodology)*, 69(2):243–268, 2007.
- [17] T. Gneiting, A. E. Raftery, A. H. ANTON Westweld, and T. Goldman. Calibrated probabilistic forecasting using ensemble model output statistics and minimum crps estimation. *Monthly Weather Review*, 133:1098–1118, 2005.
- [18] IRI. Ncep cpc pentad olr anomalies on a 0.25° lat/lon grid, 2025.
- [19] J. Knoblauch, J. Jewson and T. Damoulas. An optimization-centric view on bayes’ rule: Reviewing and generalizing variational inference. *The Journal of Machine Learning Research*, 23 (1):5789–5897, 2022.
- [20] S. Lang, E. Hölm, Bonavita M., and Y. Tremolet. A 50-member ensemble of data assimilations. *ECMWF Newsletter*, 158:27–29, 2019.
- [21] G. Liang, P. Tiwari, S. Byttner, and F. Alonso-Fernandez. Dynamic causal explanation based diffusion- variational graph neural network for spatiotemporal forecasting. *IEEE TRANSACTIONS ON NEURAL NETWORKS AND LEARNING SYSTEMS*, 36:9524–9537, 2024.
- [22] Guanjun Liu, Hui Qin, Qin Shen, Hao Lyv, Yuhua Qu, Jialong Fu, Yongqi Liu, and Jianzhong Zhou. Probabilistic spatiotemporal solar irradiation forecasting using deep ensembles convolutional shared weight long short-term memory network. *Applied Energy*, 300:117379, 2021.
- [23] Hao Liu, Junqi Liu, Tianyu Hu, and Huimin Ma. Spatio-temporal probabilistic forecasting of wind speed using transformer-based diffusion models. *IEEE Transactions on Sustainable Energy*, pages 1–13, 2025.
- [24] C. T. Lloyd. High resolution global gridded data for use in population studies. *Int. Arch. Photogramm. Remote Sens. Spatial Inf. Sci.*, XLII-4/W2:117–120, 2017.
- [25] Tianqi Ma, Lin Zhang, Xiumin Diao, and Ou Ma. Convgru in fine-grained pitching action recognition for action outcome prediction. *CoRR*, abs/2008.07819, 2020.
- [26] T. Matsubara, J. Knoblauch, Briol F. X., and C. J. Oates. Generalized bayesian inference for discrete intractable likelihood. *Journal of the American Statistical Association*, 119(547):2345–2355, 2024.

- [27] J.-M. Montero, G. Fernández-Avilès, and J. Mateu. *Spatial and Spatio-Temporal Geostatistical Modeling and Kriging*. Wiley, 2015.
- [28] M. Nguyen and A. E. D. Veraart. Spatio-temporal Ornstein–Uhlenbeck Processes: Theory, Simulation and Statistical Inference. *Scand. J. Stat.*, 44:46–80, 2017.
- [29] M. Nguyen and A. E. D. Veraart. Bridging between short-range and long-range dependence with mixed spatio-temporal Ornstein-Uhlenbeck processes. *Stochastics*, 90:1023–1052, 2018.
- [30] A. P. Nicolau, K. Dyson, D. Saah, and N. Clinton. Survey of raster data sets. In: *Cardille, J.A., Crowley, M.A., Saah, D., Clinton, N.E. (eds) Cloud-Based Remote Sensing with Google Earth Engine*. Springer, Cham, pages 41–66, 2024.
- [31] F. Nielsen and R. Nock. On the chi square and higher-order chi distances for approximating f-divergences. *IEEE Signal Processing Letters*, 21(1):10–13, 2014.
- [32] D. B. Rubin. Causal inference using potential outcomes: design, modeling, decisions. *J. Am. Stat. Assoc.*, 100:322–331, 2005.
- [33] K. Sato. *Lévy Processes and Infinitely Divisible Distributions*. Cambridge Studies in Advanced Mathematics 68. Cambridge Univ. Press, Cambridge, 2013.
- [34] Xingjian Shi, Zhourong Chen, Hao Wang, Dit-Yan Yeung, Wai-Kin Wong, and Wang-chun Woo. Convolutional LSTM network: A machine learning approach for precipitation nowcasting. *CoRR*, abs/1506.04214, 2015.
- [35] N. Wan, D. Li, and N. Hovakimyan. f-divergence variational inference. In *Advances in Neural Information Processing Systems*, pages 17370–17379, 2020.
- [36] Haomin Wen, Youfang Lin, Yutong Xia, Huaiyu Wan, Qingsong Wen, Roger Zimmermann, and Yuxuan Liang. Diffstg: Probabilistic spatio-temporal graph forecasting with denoising diffusion models. 2024.
- [37] Y. Yang, M. Jin, H. Wen, C. Zhang, Y. Liang, L. Ma, Y. Wang, C. Liu, B. Yang, Z. Xu, J. Bian, S. Pan, and A. Wen. A survey on diffusion models for time series and spatio-temporal data. arXiv:2404.18886, 2024.

# A Estimating the parameters of an STOU process and the decay rate of its $\theta$ -lex weakly dependent coefficients

To enable automatic feature extraction in MMAF-guided learning, we first need to estimate the parameters  $c$ , which we call *speed of information propagation*, and the parameter  $A$  called the *mean-reverting parameter*. Such parameters are estimated using normalized spatial and temporal variograms defined as

$$\begin{aligned}\gamma^S(u) &:= \frac{\mathbb{E}((\mathbf{Z}_t(x) - \mathbf{Z}_t(x-u))^2)}{\text{Var}(\mathbf{Z}_t(x))} = 2\left(1 - \exp\left(-\frac{Au}{c}\right)\right), \\ \gamma^T(s) &:= \frac{\mathbb{E}((\mathbf{Z}_t(x) - \mathbf{Z}_{t-s}(x))^2)}{\text{Var}(\mathbf{Z}_t(x))} = 2(1 - \exp(-As)).\end{aligned}$$

Let  $N(u)$  be the set containing all the pairs of indices at spatial distance  $u > 0$  and with same temporal instance, and  $N(s)$  be the set containing the pairs of indices where the observation times are at distance  $s > 0$  and having same spatial position. The empirical normalized spatial and temporal variograms are then defined as follows:

$$\begin{aligned}\hat{\gamma}^S(u) &= \frac{1}{|N(u)|} \sum_{i,j \in N(u)} \frac{(\mathbf{Z}_{t_i}(x_i) - \mathbf{Z}_{t_j}(x_j))^2}{\hat{\mathbf{k}}_2} \\ \hat{\gamma}^T(s) &= \frac{1}{|N(s)|} \sum_{i,j \in N(s)} \frac{(\mathbf{Z}_{t_i}(x_i) - \mathbf{Z}_{t_j}(x_j))^2}{\hat{\mathbf{k}}_2}\end{aligned}$$

where  $|N(u)|$  and  $|N(s)|$  simply represent the number of the obtained pairs, and  $\hat{\mathbf{k}}_2$  is the empirical variance

$$\hat{\mathbf{k}}_2 = \frac{1}{\tilde{D} - 1} \sum_{(t_i, x_i) \in \mathbb{T} \times \mathbb{L}} \mathbf{Z}_{t_i}^2(x_i),$$

where  $\tilde{D}$  denotes the sample size of all space-time observations in the raster dataset. By matching the empirical and the theoretical forms of the normalized variograms, we can estimate  $A$  and  $c$  by employing the estimators:

$$\mathbf{A}^* = -\tau^{-1} \log\left(1 - \frac{\hat{\gamma}^T(\tau)}{2}\right), \quad \text{and} \quad \mathbf{c}^* = -\frac{\mathbf{A}^* u}{\log\left(1 - \frac{\hat{\gamma}^S(u)}{2}\right)}. \quad (17)$$

Once we have an estimation of the parameters  $A$  and  $c$ , the next step consists in choosing the parameter  $a$ . This choice is made using a selection rule related to an estimate of the  $\theta$ -lex coefficients of the underlying field, see (11). We then need an estimate of such coefficients. For the STOU process, we can compute the  $\theta$ -lex coefficients explicitly, using Proposition 2.17 in [9]. Let  $\Lambda$  be an  $\mathbb{R}$ -valued Lévy basis with characteristic quadruplet  $(\gamma, \sigma^2, \nu, \pi)$ . If  $\int_{|x|>1} x^2 \nu(dx) < \infty$ ,  $\gamma + \int_{|x|>1} x \nu(dx) = 0$ , and for

$\psi = \psi(r) := \frac{r}{\sqrt{2(c^2+1)}}$ , then  $\mathbf{Z}$  is  $\theta$ -lex weakly dependent with coefficients

$$\begin{aligned}
\theta_{lex}(r) &\leq 2 \left( \text{Var}(\Lambda') \int_{A_0(0) \cap (A_0(\psi) \cup A_0(-\psi))} \exp(2As) \, ds \, d\xi \right)^{\frac{1}{2}} \\
&\leq 2 \left( 2 \text{Var}(\Lambda') \int_{A_0(0) \cap A_0(\psi)} \exp(2As) \, ds \, d\xi \right)^{\frac{1}{2}} \\
&= 2 \left( 2 \text{Var}(\Lambda') \int_{-\infty}^{-\frac{\psi}{2c}} \int_{\psi+cs}^{-cs} \exp(2As) \, ds \, d\xi \right)^{\frac{1}{2}} = \left( \frac{c}{A^2} \text{Var}(\Lambda') \exp\left(\frac{-A\psi}{c}\right) \right)^{\frac{1}{2}} \\
&= 2 \left( \frac{c}{A^2} \text{Var}(\Lambda') \exp\left(-\underbrace{\frac{A \min(2, c)}{c}}_{2\lambda} r\right) \right)^{\frac{1}{2}} \\
&= 2\sqrt{2 \text{Cov}(\mathbf{Z}_0(0), \mathbf{Z}_0(r \min(2, c)))} := \exp(-\lambda r),
\end{aligned}$$

where  $\lambda > 0$ .

By estimating the parameter  $\lambda$ , we then get an estimation of the coefficients. This is done using the following plug-in estimator.

$$\lambda^* = \frac{A^* \min(2, c^*)}{2c^*}. \quad (18)$$

## B Dependence Structure of the stochastic process $\mathbf{S}$

In this section, we prove that the following statement

**Lemma B.1.** *The stochastic process  $\mathbf{S} = (\mathbf{S}_i)_{i \in \mathbb{Z}} := (\mathbf{X}_i, \mathbf{Y}_i)_{i \in \mathbb{Z}}$  related to the position  $x^*$  and with values in  $\mathbb{R}^{D+1}$ , as defined in Section 2.2, is  $\theta$ -weakly dependent.*

$\theta$ -weak dependence is a dependence notion that holds for causal stochastic processes. The relationship between  $\theta$  and  $\theta$ -lex weak dependence is thoroughly analyzed in [10]. We give the definition of  $\theta$ -weak dependence for stochastic processes defined on the index set  $\mathbb{Z}$  below.

**Definition B.2.** *Let  $\mathbf{S} = (\mathbf{S}_i)_{i \in \mathbb{Z}}$  be a  $\mathbb{R}^{D+1}$ -valued stochastic process. Then  $\mathbf{S}$  is called  $\theta$ -weakly dependent if*

$$\theta(k) = \sup_{u \in \mathbb{N}} \theta_u(k) \xrightarrow{k \rightarrow \infty} 0$$

where

$$\theta_u(k) = \sup \left\{ \frac{|\text{Cov}(F(\mathbf{S}_\Gamma), G(\mathbf{S}_j))|}{\|F\|_\infty \text{Lip}(G)}, F \in \mathcal{G}_u^*, G \in \mathcal{G}_1, \Gamma, j \right\}$$

where  $\mathcal{G}_u^*$  represents the set of the bounded functions on  $\mathbb{R}^{u(D+1)}$ ,  $\mathcal{G}_1$  the set of bounded and Lipschitz functions on  $\mathbb{R}^{(D+1)}$ ,  $\Gamma = \{i_1, \dots, i_u\} \subset \mathbb{Z}$ ,  $j \in \mathbb{Z}$  such that  $i_1 \leq i_2 \leq \dots \leq i_u + k = j$ . We call  $(\theta(k))_{k \in \mathbb{R}^+}$  the  $\theta$ -coefficients.

Before giving the proof of Proposition B.1, let us remind the structure of the random vector  $\mathbf{S} := (\mathbf{S}_i)_{i \in \mathbb{Z}}$ .

$$\mathbf{S}_i = (\mathbf{X}_i, \mathbf{Y}_i) = (\mathbf{Z}_{i_1}(x_1), \dots, \mathbf{Z}_{i_D}(x_D), \mathbf{Z}_{t_0+ia}(x^*))$$

where  $(i_s, x_s) \in I(t_0 + ia, x^*)$  and  $(i_s, x_s) <_{lex} (i_{s+1}, x_{s+1})$  for all  $s = 1, \dots, D$ .

We define now a *truncation for the random vector*  $\mathbf{S}_j$  as follows, let  $\psi := \psi(r)$  for  $r \in \mathbb{R}_+$

$$\mathbf{S}_j^{(\psi)} = (\mathbf{Z}_{j_1}^{(\psi)}(x_1), \dots, \mathbf{Z}_{j_D}(\psi)(x_D), \mathbf{Z}_{t_0+ia}(\psi)(x^*)).$$

Let us call  $(t, x)$  a generic spatial-time index appearing in the definition of  $\mathbf{S}_j$ , then

$$\mathbf{Z}_t^{(\psi)}(x) = \int_{A_t(x) \cap V_t^\psi(x)} \exp(-A(t-s)) \Lambda(ds, d\xi),$$

with  $V_t^\psi(x)$  a set such that

- $|V_t^\psi(x)| \rightarrow \infty$  as  $r \rightarrow \infty$ ,
- $\mathbb{E}[|\mathbf{Z}_t(x) - \mathbf{Z}_t^{(\psi)}(x)|] \rightarrow 0$  as  $r \rightarrow \infty$ , and
- such that the random vectors  $\mathbf{S}_l$  and  $\mathbf{S}_j^{(\psi)}$  are independent for  $l < j$  and represent marginals of the field  $\mathbf{Z}$  at distance  $r = (j-l)a - p$ .

A formal definition of the sets  $V_t^\psi(x)$  can be found in [10], and consists of a truncation of the ambit set in the definition of the random field. The property of independence between random vectors  $\mathbf{S}_l$  and  $\mathbf{S}_j^{(\psi)}$  for  $l < j$  follows from the property of the Lévy basis.

In the following, Lipschitz continuous is understood to mean globally Lipschitz. For  $u \in \mathbb{N}$ ,  $\mathcal{G}_1$  is the class of bounded, Lipschitz continuous functions from  $\mathbb{R}^{D+1}$  to  $\mathbb{R}$  with respect to the distance  $\|\cdot\|_1$  and define the Lipschitz constant as

$$Lip(h) = \sup_{x \neq y} \frac{|h(x) - h(y)|}{\|x - y\|_1}.$$

*Proof.* For  $F \in \mathcal{G}_u^*$ ,  $G \in \mathcal{G}_1$ , and for  $u \in \mathbb{N}$ ,  $i_1 \leq i_2 \leq \dots \leq i_u < i_u + k = j$

$$|Cov(F(\mathbf{S}_{i_1}, \dots, \mathbf{S}_{i_u}), G(\mathbf{S}_j))| \leq |Cov(F(\mathbf{S}_{i_1}, \dots, \mathbf{S}_{i_u}), G(\mathbf{S}_j) - G(\mathbf{S}_j^{(\psi)}))| \quad (19)$$

$$+ |Cov(F(\mathbf{S}_{i_1}, \dots, \mathbf{S}_{i_u}), G(\mathbf{S}_j^{(\psi)}))| \quad (20)$$

We have that 20 is equal to zero because of the independence of the random vectors  $(\mathbf{S}_{i_1}, \dots, \mathbf{S}_{i_u})$  and  $\mathbf{S}_j$ . The term (19) is less than or equal to

$$2\|F\|_\infty Lip(G)(\mathbb{E}[\|\mathbf{S}_j - \mathbf{S}_j^{(\psi)}\|_1]) \quad (21)$$

$$\leq 2\|F\|_\infty Lip(G) \underbrace{(D+1)(\mathbb{E}[|\mathbf{Z}_t(x) - \mathbf{Z}_t^{(\psi)}(x)|])}_{\theta(k)}. \quad (22)$$

Because  $r = ka - p$  in relation to the marginals used in (19), and the properties of the truncation for the random vector  $\mathbf{S}_j$ ,  $\theta(k) \rightarrow 0$  for  $k \rightarrow \infty$ , proving that  $\mathbf{S}$  is a  $\theta$ -weakly dependent process. ■

## C Training algorithm convergence

For each spatial position, we apply Algorithm 2 and study its convergence with respect to the number of epochs which are setup to be a maximum of 60 in the GAU and NIG framework, and 5,000 in the OLR one.

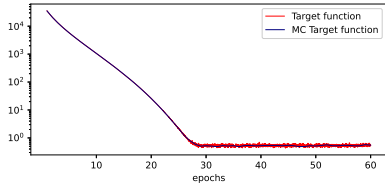
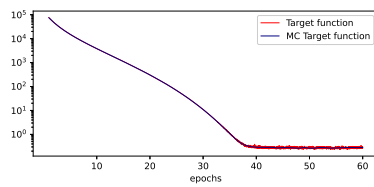
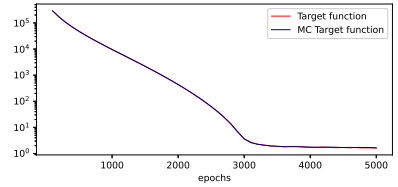


Figure  
Gau,  $[300^2], \pi \sim N(0, 1/110)$



7: Figure  
NIG,  $[300^2], \pi \sim N(0, 1/210)$



8: Figure  
OLR,  $[300^2], \pi \sim N(0, 1/90)$  9:

Figures 7, 8, and 9 show the convergence of the target function for an exemplary stochastic feed-forward neural network used in our empirical study. Note that the curves in Figures 7, 8, and 9 report the average values of the target function over the analyzed spatial positions.